


Please cite the Published Version

Hollingsworth, EH, Sparkes, RB , Self-Trail, JM, Foster, GL and Inglis, GN (2024) Enhanced petrogenic organic carbon oxidation during the Paleocene-Eocene thermal maximum. *Geochemical Perspectives Letters*, 33. pp. 1-6. ISSN 2410-339X

DOI: <https://doi.org/10.7185/geochemlet.2444>

Publisher: European Association of Geochemistry

Version: Published Version

Downloaded from: <https://e-space.mmu.ac.uk/637346/>

Usage rights:  [Creative Commons: Attribution-Noncommercial-No Derivative Works 4.0](https://creativecommons.org/licenses/by-nc-nd/4.0/)

Additional Information: This is an open access article which first appeared in *Geochemical Perspectives Letters*

Data Access Statement: All the new data in this study are available in the Supporting Information.

Enquiries:

If you have questions about this document, contact openresearch@mmu.ac.uk. Please include the URL of the record in e-space. If you believe that your, or a third party's rights have been compromised through this document please see our Take Down policy (available from <https://www.mmu.ac.uk/library/using-the-library/policies-and-guidelines>)

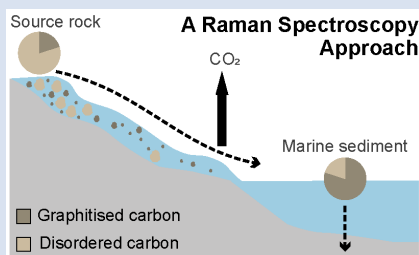
Enhanced petrogenic organic carbon oxidation during the Paleocene-Eocene thermal maximum

E.H. Hollingsworth^{1*}, R.B. Sparkes², J.M. Self-Trail³, G.L. Foster¹, G.N. Inglis¹



<https://doi.org/10.7185/geochemlet.2444>

Abstract



The Paleocene-Eocene thermal maximum (PETM; ~56 Ma) is a hyperthermal event associated with the rapid input of carbon into the ocean-atmosphere system. The oxidation of petrogenic organic carbon (OC_{petro}) may have released additional carbon dioxide (CO_2), thereby prolonging the PETM. However, proxy-based estimates of OC_{petro} oxidation are unavailable due to the lack of suitable techniques. Raman spectroscopy is used to evaluate OC_{petro} oxidation in modern settings. For the first time, we explore whether Raman spectroscopy can evaluate OC_{petro} oxidation during the PETM. In the mid-Atlantic Coastal Plain, there is a shift from disordered to graphitised carbon. This is consistent with enhanced oxidation of disordered OC_{petro} and intensified physical erosion. In the Arctic Ocean, the distribution of graphitised carbon

vs. disordered carbon does not change, suggesting limited variability in weathering intensity. Overall, this study provides the first evidence of increased OC_{petro} oxidation during the PETM, although it was likely not globally uniform. Our work also highlights the utility of Raman spectroscopy as a novel tool to reconstruct OC_{petro} oxidation in the past.

Received 21 June 2024 | Accepted 4 November 2024 | Published 25 November 2024

Introduction

At the Paleocene-Eocene boundary, an abrupt carbon cycle perturbation gave rise to a global warming event (~4–6 °C; Tierney *et al.*, 2022), known as the Paleocene-Eocene thermal maximum (PETM; ~56 Ma). The initial flux of carbon occurred within ~3–21 kyr (the ‘onset’ of the PETM; see Kirtland Turner, 2018 and references therein), yet the PETM persisted for a further 170 ± 30 kyr (the ‘body’ of the PETM; Zeebe and Lourens, 2019). The long duration of the PETM can be reproduced in carbon cycle models but requires a continuous or additional source of carbon into the ocean-atmosphere system (*e.g.*, Bowen, 2013). Proposed mechanisms for the additional source include the slow dissociation of oceanic methane hydrates (*e.g.*, Zeebe, 2013), pulsed emissions from hydrothermal vent complexes (see Jin *et al.*, 2024 and references therein), and the oxidation of soil organic carbon (*e.g.*, Bowen, 2013) or petrogenic organic carbon (OC_{petro}) (Lyons *et al.*, 2019).

Biomarker thermal maturity ratios can fingerprint OC_{petro} that has been subject to relatively low burial temperature (<165 °C). Changes in biomarker thermal maturity ratios from a global compilation of shallow-marine sediments indicate greater delivery of OC_{petro} into the ocean during the PETM (Lyons *et al.*, 2019; Hollingsworth *et al.*, 2024). Based on modern observations (*e.g.*, Hilton and West, 2020; Soulet *et al.*, 2021), it is likely that the increased erosion rates and higher temperatures during the PETM enhanced OC_{petro} oxidation. However, constraining the fraction of OC_{petro} that was oxidised to CO_2

(*i.e.* the oxidation efficiency) remains challenging in the geologic record. In order to calculate the mass of OC_{petro} -derived CO_2 released during the body of the PETM, Lyons *et al.* (2019) used the present day lower and upper bounds in oxidation efficiency (15–85 %; Bouchez *et al.*, 2010; Hilton *et al.*, 2014). This resulted in a wide range of estimates that span two orders of magnitude (10^2 – 10^4 PgC; Lyons *et al.*, 2019). To reduce the uncertainty, new techniques are required to determine OC_{petro} oxidation efficiency in the past. This will help reveal whether OC_{petro} oxidation is an important positive feedback mechanism during hyperthermals, and thus its potential role in future climate change.

Here, we explore the utility of Raman spectroscopy as a novel tool to reconstruct OC_{petro} oxidation in the geologic record. Raman spectroscopy is a non-destructive technique that assesses nm-scale differences in the crystallinity of carbonaceous materials. This enables the distinction between highly crystalline (*i.e.* graphite) to amorphous (*i.e.* disordered) carbon, and can therefore detect OC_{petro} that formed at burial temperatures up to 650 °C (Beysac *et al.*, 2002). As the porous structure of disordered carbon makes it more susceptible to oxidation, a shift towards a dominance of graphitised carbon downstream has been suggested to indicate high OC_{petro} oxidation efficiency (Fig. 1). This has been used to evaluate OC_{petro} oxidation in modern settings (*e.g.*, Galy *et al.*, 2008; Bouchez *et al.*, 2010). However, this approach has rarely been applied in a geological context. Here, we employ Raman spectroscopy to identify OC_{petro} in PETM-aged sediments, and evaluate changes in OC_{petro} oxidation during the PETM.

1. School of Ocean and Earth Science, University of Southampton, Southampton, UK
2. Department of Natural Sciences, Manchester Metropolitan University, Manchester, UK
3. U.S. Geological Survey, Florence Bascom Geoscience Center, Reston, VA, USA
* Corresponding author (email: e.hollingsworth@soton.ac.uk)

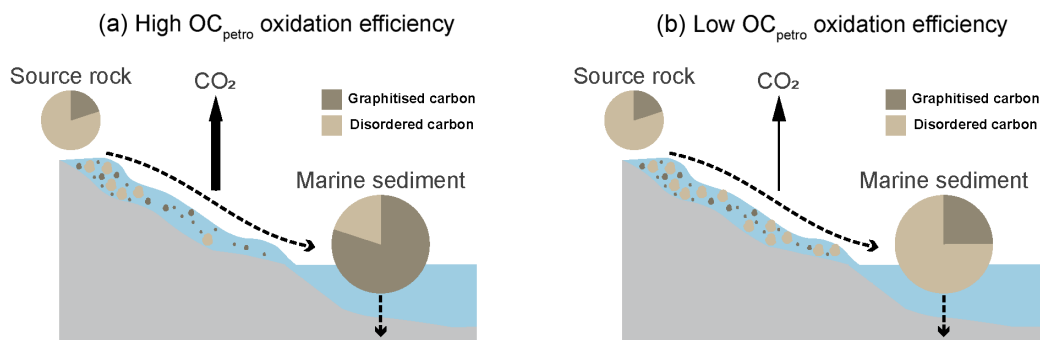


Figure 1 A simplified schematic illustrating the Raman spectroscopy approach to evaluating OC_{petro} oxidation. Marine sediment composition with (a) a dominance of graphitised carbon (dark brown) and (b) graphitised and disordered carbon (light brown), indicating a high and low OC_{petro} oxidation efficiency, respectively. Given that OC_{petro} oxidation is a source of CO_2 , this correlates with a (a) high and (b) low CO_2 flux.

Material and Methods

We investigated two shallow-marine sites that exhibit higher OC_{petro} mass accumulation rates (MAR) during the PETM (Hollingsworth *et al.*, 2024). The South Dover Bridge (SDB) core was drilled in the Salisbury Embayment (mid-Atlantic Coastal Plain; Fig. S-1) and shows a drastic increase in OC_{petro} delivery during the PETM (Lyons *et al.*, 2019). International Ocean Drilling Program Expedition 302 Site M0004A (ACEX; Fig. S-1), is located at the Lomonosov Ridge (central Arctic Ocean) and indicates minimal change in organic carbon source(s) during the PETM (Hollingsworth *et al.*, 2024).

We follow the Raman spectroscopy methodology outlined in Sparkes *et al.* (2013), which was specifically developed to facilitate the analyses of sedimentary rocks. Overall, 36 samples from SDB and 12 samples from ACEX were processed and analysed with an InVia Raman spectrometer (Renishaw). Firstly, wet sediments were either freeze dried or placed in a 50 °C oven overnight (Table S-2). The samples were then ground to a fine powder with a Planetary Mill Pulverisette 5 (Fritsch), for 2 min at 300 rpm. Between samples, the agate mill and balls were cleaned with isopropanol. The homogenised samples were then compressed between two glass slides to create a 1 cm² area which can be rastered under a 50x magnification microscope. The slides were systematically scanned by traversing at regular spaced intervals. All carbonaceous particles were first determined by brief exposure to a 514 nm Ar-ion laser (2 s; measurement window 1050–1915 cm⁻¹). Those confirmed were further inspected and photographed prior to a final spectrum being measured using longer exposure (60 s; measurement window 800–2200 cm⁻¹). Laser power was kept low enough (estimated to be <6 mW) to cause no noticeable thermal alterations to the targets. To increase the chance that the data is representative of the population, 10 spectra were collected for each sample. The peaks in each spectrum were fitted using an updated script (<https://github.com/robertsparkes/raman-fitting/releases/tag/v1.1.5>) of the automated process described in Sparkes *et al.* (2013), and manually checked for inconsistencies.

Results

In total, 360 spectra from SDB and 120 spectra from ACEX were collected. The automated process resulted in only 7 spectra from SDB and 1 spectrum from ACEX being excluded due to a noise-to-signal ratio greater than 1:3. In previous studies, spectra were characterised as either: (i) highly graphitised carbon, (ii) mildly graphitised carbon, (iii) intermediate carbon, or (iv) disordered

carbon (Sparkes *et al.*, 2013). Spectra from highly graphitised carbon have a single sharp peak at 1580 cm⁻¹ (G peak; Fig. 2e). Disordered carbon has a wider 'G band' at approximately 1600 cm⁻¹, produced by a convolution of the G (1580 cm⁻¹) and D2 (1620 cm⁻¹) peaks, alongside other peaks signifying disorder (D1; 1350 cm⁻¹, D3; 1500 cm⁻¹, and D4; 1200 cm⁻¹; Fig. 2f). Our data suggests a bimodal distribution (Fig. 2e,f), and as such, spectra were categorised as either graphitised or disordered carbon (Fig. 2a–d, Tables S-1 and S-2). This separation was based on peak burial temperatures, which were calibrated using the R2 and RA2 peak area ratio, and not the sum of peak width (G + D1 + D2) (see Sparkes *et al.*, 2013).

At SDB, there is a mixture of both graphitised and disordered carbon in the pre-PETM interval (including the pre-onset excursion; POE) and 'Core' PETM (including the onset, body, and Recovery interval) (Fig. 2a,b). Compared to the pre-PETM, the PETM exhibits a statistically highly significant ($P < 0.001$) increase in the mean percentage of graphitised carbon (33 %; Fig. S-2a). However, this shift does not occur until ~1.5 m above the onset of the PETM (Fig. 3b). At ACEX, there is a dominance of disordered carbon in the pre-PETM interval and Core PETM (Fig. 2c,d), and no statistically significant ($P \geq 0.1$) change throughout the record (Fig. 4b, Fig. S-2c). Both sites show a higher percentage of graphitised carbon in the Recovery and post-PETM intervals than in the pre-PETM interval (Fig. S-2a,c).

To assess whether our semi-quantitative method (*i.e.* 10 spectra *per* sample) can accurately represent the population, four samples from SDB were analysed in duplicate (Fig. 3b, Table S-1). With the exception of 202.37 m (s.d. = 35 %), the measurements yielded similar values (average s.d. = 7 %). However, interpretations of small scale variability should be made with caution and we suggest that future studies increase the number of spectra *per* sample.

Discussion

Fingerprinting OC_{petro} delivery during the PETM. Raman spectroscopy has most commonly been used to fingerprint OC_{petro} in modern river catchments and continental shelves (*e.g.*, Galy *et al.*, 2008; Bouchez *et al.*, 2010; Sparkes *et al.*, 2018, 2020). Thus, we first compare our results to published biomarker thermal maturity ratios from the same PETM-aged shallow-marine cores (Lyons *et al.*, 2019; Hollingsworth *et al.*, 2024). The C_{31} homohopane 22S/(22S + 22R) ratio is plotted alongside the percentage of graphitised carbon at SDB (Figs. 3c, S-2b) and ACEX (Figs. 4c, S-2d). Higher C_{31} S/(S + R) values suggest greater

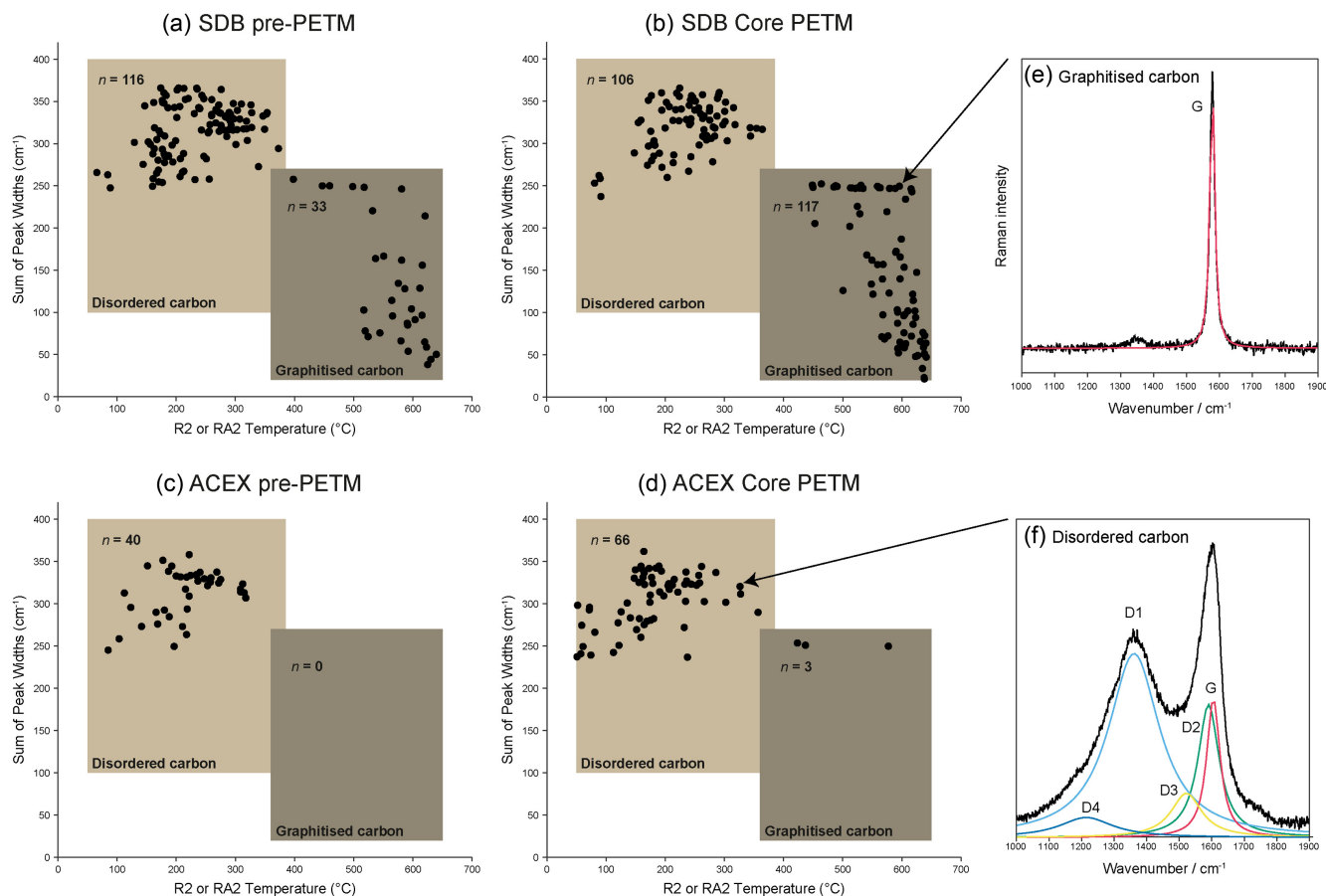


Figure 2 ‘Sparkes’ plots combining data from the pre-PETM interval (including the pre-onset excursion; POE) vs. Core PETM (including the onset, body, and Recovery interval; see Hollingsworth *et al.*, 2024 and references therein), at (a–b) SDB and (c–d) ACEX. The spectra are categorised into either graphitised carbon (dark brown) or disordered carbon (light brown). Examples of Raman spectra (black) with fitted peaks (coloured) for (e) graphitised carbon, from a SDB sample at 200.28 m, and (f) disordered carbon, from an ACEX sample at 385.11 mcd. Spectra have had a linear background removed during the automated process, and the fitted peaks include: G (1580 cm^{-1}), D1 (1350 cm^{-1}), D2 (1620 cm^{-1}), D3 (1500 cm^{-1}), and D4 (1200 cm^{-1}) (Sparkes *et al.*, 2013).

delivery of OC_{petro} with values closer to 0.6 indicating input of OC_{petro} formed during early stages of the oil window.

Overall, there are similarities between the percentage of graphitised carbon and the $\text{C}_{31} \text{S}/(\text{S} + \text{R})$ ratio at both sites, whereby SDB exhibits large fluctuations (Fig. 3) and ACEX shows relatively low and stable values (Fig. 4). At SDB, the percentage of graphitised carbon and $\text{C}_{31} \text{S}/(\text{S} + \text{R})$ ratio increases between the pre-PETM interval and both the POE and PETM intervals (Fig. S-2a,b). However, a lag within the PETM interval in the percentage of graphitised carbon (Fig. 3b), $\text{C}_{31} \text{S}/(\text{S} + \text{R})$ ratio (Fig. 3c), and bulk carbon isotope of organic carbon ($\delta^{13}\text{C}_{\text{org}}$), suggests a delayed response of $\sim 10\text{--}20$ kyr (Lyons *et al.*, 2019). This confirms that Raman spectroscopy can be applied to fingerprint OC_{petro} delivery in the past, and could be particularly powerful in permitting the inclusion of study sites with post-depositional diagenesis (Sparkes *et al.*, 2020). Our new data supports previous findings indicating enhanced OC_{petro} delivery at SDB (Lyons *et al.*, 2019) and no drastic changes in organic carbon source(s) at ACEX (Hollingsworth *et al.*, 2024) during the PETM. Assuming that the graphitised carbon and thermally mature biomarkers at SDB came from the same source, the increase in graphitised OC_{petro} MAR during the PETM is calculated to be $2 \times 10^{-2} \text{ g cm}^{-2} \text{ kyr}^{-1}$ (based on Hollingsworth *et al.*, 2024).

Characterising and identifying the potential sources of OC_{petro} . Kopp *et al.* (2009) initially hypothesised that Cretaceous-aged upland deposits, such as the Potomac

Group, could have been a source of sediment to the Salisbury Embayment during the PETM. Indeed, similarities were found with the biomarker thermal maturity ratios from the Raritan Formation of the upper Potomac Group and the PETM-aged SDB core (Lyons *et al.*, 2019). In addition, the $\delta^{13}\text{C}_{\text{org}}$ values and source rock properties (*e.g.*, T_{max}) are comparable (Lyons *et al.*, 2019). As there is a correlation between the percentage of graphitised carbon (Figs. 3b, S-2a) and the $\text{C}_{31} \text{S}/(\text{S} + \text{R})$ ratios (Figs. 3c, S-2b), this suggests that the graphitised OC_{petro} may have also been sourced from the Raritan Formation. However, the presence of graphitised OC_{petro} implies burial temperatures ($\sim 350\text{--}650$ °C; Beyssac *et al.*, 2002) that should severely diminish or completely destroy biomarkers. Therefore, the graphitised OC_{petro} was likely reworked into the Raritan Formation and subsequently re-exhumed alongside the thermally mature biomarkers during the PETM. This is consistent with present day observations of graphite particles surviving transport over thousands of kilometres (*e.g.*, Galy *et al.*, 2008) and persisting over multiple erosion cycles (*e.g.*, Sparkes *et al.*, 2020). Decoupling between the percentage of graphitised carbon and the $\text{C}_{31} \text{S}/(\text{S} + \text{R})$ ratios during the POE could thus be reflecting two distinct sources of OC_{petro} (Figs. 3b,c, S-2a,b).

At ACEX, the relative abundance of disordered carbon (Figs. 4b, S-2c) and low $\text{C}_{31} \text{S}/(\text{S} + \text{R})$ values (Figs. 4c, S-2d) throughout the record indicates that the OC_{petro} is derived from a more thermally immature source rock (*i.e.* protolith). This is

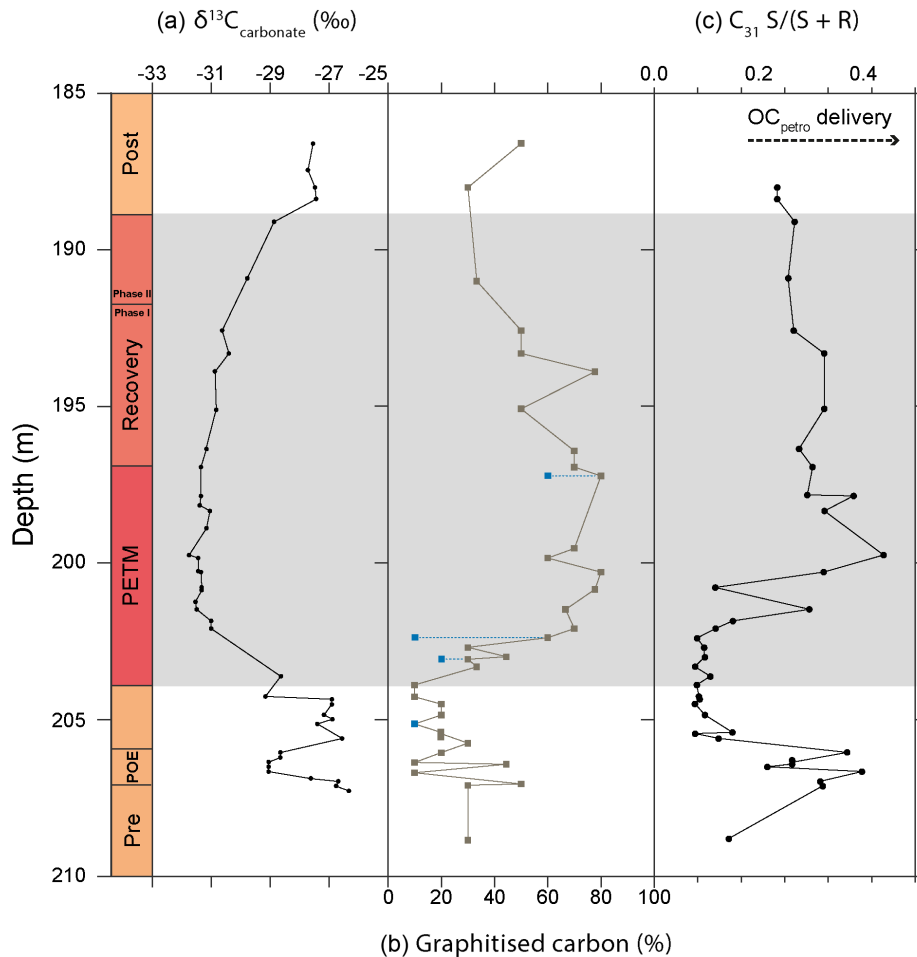


Figure 3 The SDB record of (a) bulk sediment $\delta^{13}\text{C}$ of carbonates ($\delta^{13}\text{C}_{\text{carbonates}}$; Lyons *et al.*, 2019), (b) percentage graphitised carbon (this study), and (c) C_{31} homohopane 22S/(22S + 22R) ratio (Lyons *et al.*, 2019). The blue symbols within panel (b) are the duplicate measurements. The time intervals are as follows: pre-PETM, PETM (onset/body), Recovery Phase I, Recovery Phase II, and post-PETM, based on Hollingsworth *et al.* (2024) and references therein. The POE in the pre-PETM interval is isolated using the definition from Babila *et al.* (2022).

consistent with the excellent preservation of pollen and spores (Sluijs *et al.*, 2008), and the presence of biomarkers diagnostic of peats and/or lignite deposits (e.g., C_{31} $\alpha\beta$ hopanes; Hollingsworth *et al.*, 2024), in these sediments. The dominance of disordered carbon also implies limited availability of graphite-rich source rocks.

Evaluating OC_{petro} oxidation during the PETM. The mid-Atlantic Coastal Plain during the PETM has been referred to as the ‘Appalachian Amazon’ due to similarities with sediments from the modern Amazon shelf, including features indicative of hyperpycnal flow (Self-Trail *et al.*, 2017), and the presence of kaolinite (Gibson *et al.*, 2000) and magnetofossils (see Kopp *et al.*, 2009 and references therein). Present day observations of two Amazon tributaries show the preferential oxidation of the less recalcitrant disordered OC_{petro} and a consequential relative increase in graphite downstream (Bouchez *et al.*, 2010). The Amazon is mostly supplied by low grade metamorphic rocks from the Andes, which are subject to a long residence time within the extensive meandering rivers typical of large catchments. This results in the estimated loss of up to $\sim 90\%$ of OC_{petro} during transport (Bouchez *et al.*, 2010; see Dellinger *et al.*, 2023 and references therein). The progressive shift towards more graphitised carbon along the land to sea transect is also seen in modern rivers that have a contribution of high grade metamorphic rocks, such as in the Himalayas (Beyssac *et al.*, 2004). However, the Himalayas have a more efficient sediment routing

system that promotes burial of OC_{petro} in the Bengal Fan (Galy *et al.*, 2007).

As the Amazon shelf is the closest analogue for the mid-Atlantic Coastal Plain, we argue that the shift from a dominance of disordered to graphitised carbon at SDB represents enhanced oxidation of disordered OC_{petro} during the PETM. We note that the oxidation and/or deposition of OC_{petro} can also occur in floodplains (e.g., Scheingross *et al.*, 2021). However, this would lead to the loss of all types of OC_{petro} from the fluvial load, thus maintaining an equal distribution of graphitised carbon *vs.* disordered carbon between the pre-PETM and PETM intervals. An average $\sim 5^\circ\text{C}$ of warming during the PETM (Tierney *et al.*, 2022) may have also caused OC_{petro} oxidation to increase by one fold, based on observations made by Soulet *et al.* (2021) in modern river catchments.

At SDB, there is a pronounced ~ 20 fold increase in linear sedimentation rates, and higher OC_{petro} MAR, during the PETM (Lyons *et al.*, 2019). Given the widespread evidence for intense precipitation events (see Carmichael *et al.*, 2017 and references therein) and exacerbated erosion rates (e.g., John *et al.*, 2008), greater exhumation of graphitised OC_{petro} can also explain the shift from a dominance of disordered to graphitised carbon. For example, a more active palaeo-Potomac river could have sourced new graphite-rich rocks from regions in the Appalachian Mountains. The lower magnitude change in the relative abundance of graphitised carbon during the POE would

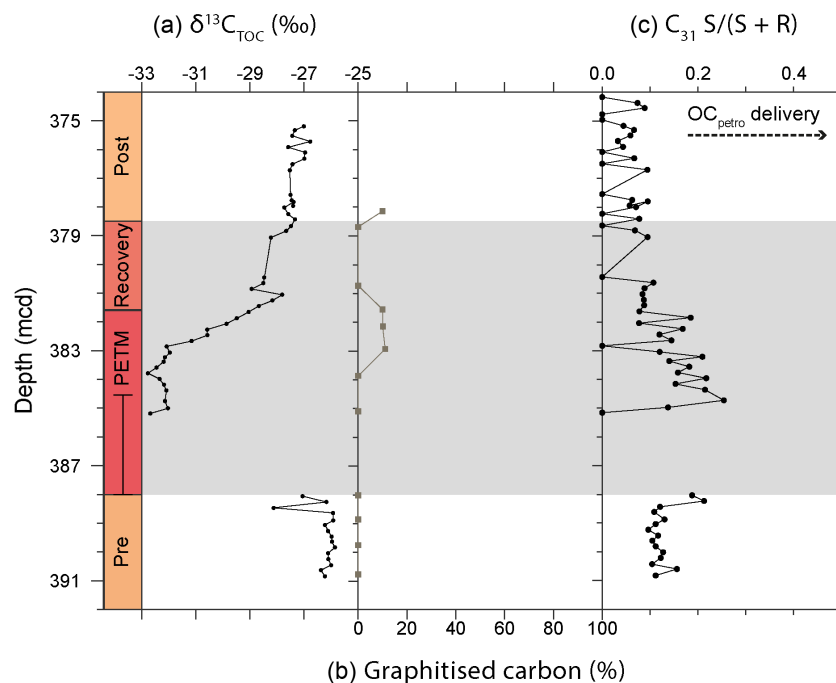


Figure 4 The ACEX record of (a) bulk sediment $\delta^{13}\text{C}$ of total organic carbon ($\delta^{13}\text{C}_{\text{TOC}}$; Elling *et al.*, 2019), (b) percentage graphitised carbon (this study), and (c) C_{31} homohopane 22S/(22S + 22R) ratio (Hollingsworth *et al.*, 2024). The time intervals are as follows: pre-PETM, PETM (onset/body), Recovery, and post-PETM, based on Hollingsworth *et al.* (2024) and references therein. Note the core gap from ~388–384.5 mcd (Sluijs *et al.*, 2006).

therefore imply lower oxidation efficiency and/or abated physical erosion (Figs. 3b, S-2a). At ACEX, intense precipitation may have countered warming-induced OC_{petro} oxidation by decreasing residence time in the rivers and/or amplifying floodplain storage. Higher sedimentation rates also promotes the burial and preservation of organic matter (*e.g.*, Galy *et al.*, 2007). However, the limited presence of graphite in this system could suppress signals that indicate changes in the oxidation of disordered OC_{petro} .

Overall, Raman spectroscopy reveals that OC_{petro} oxidation acted as a positive feedback mechanism in the mid-Atlantic Coastal Plain during the PETM. However, this change is not observed with smaller scale carbon cycle perturbations such as the POE (see Babila *et al.*, 2022 and references therein), whilst data from the Arctic Ocean suggests that enhanced OC_{petro} oxidation may not be globally uniform. Quantifying oxidation efficiency and subsequent CO_2 release *via* Raman spectroscopy requires ground truthing our approach in modern settings with different weathering intensities. It is also important to constrain the composition of the source rock(s), and understand the influence of other abiotic (*e.g.*, rainfall type, temperature, O_2 availability, and mineral association) and biotic (*e.g.*, microbial activity) processes on oxidation efficiency (*e.g.*, see Hilton and West, 2020 and references therein; Soulet *et al.*, 2021). Crucially, this study exemplifies the utility of Raman spectroscopy to fingerprint OC_{petro} delivery and – when combined with biomarker thermal maturity ratios – expands the type of OC_{petro} detected and thus sites that can be investigated. It also highlights the potential for Raman spectroscopy to reconstruct OC_{petro} oxidation in the geological past.

Acknowledgements

EHH acknowledges funding from NERC (Grant NE/S007210). GNI is supported by a GCRF Royal Society Dorothy Hodgkin Fellowship (DHF/R1/191178) with additional support *via* the

Royal Society (RF\ERE\231019, RF\ERE\210068). This research used samples provided by the U.S. Geological Survey (USGS) and the International Ocean Drilling Program (IODP). Any use of trade, firm, or product names is for descriptive purposes only and does not imply endorsement by the U.S. Government. We are grateful to Hayley Andrews from the Manchester Metropolitan University (MMU) for support with the Raman spectrometer. We thank Bart van Dongen for proposing this potential collaboration at the 2023 British Organic Geochemistry Meeting (BOGS). We also thank Bob Hilton and an anonymous reviewer for providing constructive feedback that greatly improved the manuscript.

Editor: Claudine Stirling

Additional Information

Supplementary Information accompanies this letter at <https://www.geochemicalperspectivesletters.org/article2444>.

Data Availability Statement

All the new data in this study are available in the Supporting Information.



© 2024 The Authors. This work is distributed under the Creative Commons Attribution Non-Commercial No-Derivatives 4.0

License, which permits unrestricted distribution provided the original author and source are credited. The material may not be adapted (remixed, transformed or built upon) or used for commercial purposes without written permission from the author. Additional information is available at <https://www.geochemicalperspectivesletters.org/copyright-and-permissions>.

Cite this letter as: Hollingsworth, E.H., Sparkes, R.B., Self-Trail, J.M., Foster, G.L., Inglis, G.N. (2024) Enhanced petrogenic organic carbon oxidation during the Paleocene-Eocene thermal maximum. *Geochem. Persp. Let.* 33, 1–6. <https://doi.org/10.7185/geochemlet.2444>

References

- BABILA, T.L., PENMAN, D.E., STANDISH, C.D., DOUBRAWA, M., BRALOWER, T.J., ROBINSON, M.M., SELF-TRAIL, J.M., SPEJER, R.P., STASSEN, P., FOSTER, G.L., ZACHOS, J.C. (2022) Surface ocean warming and acidification driven by rapid carbon release precedes Paleocene-Eocene Thermal Maximum. *Science Advances* 8, eabg1025. <https://doi.org/10.1126/sciadv.abg1025>
- BEYSSAC, O., GOFFÉ, B., CHOPIN, C., ROUZAUD, J.N. (2002) Raman spectra of carbonaceous material in metasediments: A new geothermometer. *Journal of Metamorphic Geology* 20, 859–871. <https://doi.org/10.1046/j.1525-1314.2002.00408.x>
- BEYSSAC, O., BOLLINGER, L., AVOUAC, J.P., GOFFÉ, B. (2004) Thermal metamorphism in the lesser Himalaya of Nepal determined from Raman spectroscopy of carbonaceous material. *Earth and Planetary Science Letters* 225, 233–241. <https://doi.org/10.1016/j.epsl.2004.05.023>
- BOUCHEZ, J., BEYSSAC, O., GALY, V., GAILLARDET, J., FRANCE-LANORD, C., MAURICE, L., MOREIRA-TURCO, P. (2010) Oxidation of petrogenic organic carbon in the Amazon floodplain as a source of atmospheric CO₂. *Geology* 38, 255–258. <https://doi.org/10.1130/G30608.1>
- BOWEN, G.J. (2013) Up in smoke: A role for organic carbon feedbacks in Paleogene hyperthermals. *Global and Planetary Change* 109, 18–29. <https://doi.org/10.1016/j.gloplacha.2013.07.001>
- CARMICHAEL, M.J., INGLIS, G.N., BADGER, M.P.S., NAAFS, B.D.A., BEHROOZ, L., REMMELZWAAL, S., MONTEIRO, F.M., ROHRSEN, M., FARNSWORTH, A., BUSS, H.L., DICKSON, A.J., VALDES, P.J., LUNT, D.J., PANCOST, R.D. (2017) Hydrological and associated biogeochemical consequences of rapid global warming during the Paleocene-Eocene Thermal Maximum. *Global and Planetary Change* 157, 114–138. <https://doi.org/10.1016/j.gloplacha.2017.07.014>
- DELLINGER, M., HILTON, R.G., BARONAS, J.J., TORRES, M.A., BURT, E.I., CLARK, K.E., GALY, V., CCAHUANA QUISEPE, A.J., WEST, A.J. (2023) High rates of rock organic carbon oxidation sustained as Andean sediment transits the Amazon foreland- floodplain. *Proceedings of the National Academy of Sciences* 120. <https://doi.org/10.1073/pnas.2306343120>
- ELLING, F.J., GOTTSCHALK, J., DOEANA, K.D., KUSCH, S., HURLEY, S.J., PEARSON, A. (2019) Archaeal lipid biomarker constraints on the Paleocene-Eocene carbon isotope excursion. *Nature Communications* 10, 1–10. <https://doi.org/10.1038/s41467-019-12553-3>
- GALY, V., FRANCE-LANORD, C., BEYSSAC, O., FAURE, P., KUDRASS, H., PALHOL, F. (2007) Efficient organic carbon burial in the Bengal fan sustained by the Himalayan erosional system. *Nature* 450, 407–410. <https://doi.org/10.1038/nature06273>
- GALY, V., BEYSSAC, O., FRANCE-LANORD, C., EGLINTON, T. (2008) Recycling of Graphite During Himalayan Erosion: A Geological Stabilization of Carbon in the Crust. *Science* 322, 943–945. <https://doi.org/10.1126/science.1161408>
- GIBSON, T.G., BYBELL, L.M., MASON, D.B. (2000) Stratigraphic and climatic implications of clay mineral changes around the Paleocene/Eocene boundary of the northeastern US margin. *Sedimentary Geology* 134, 65–92. [https://doi.org/10.1016/S0037-0738\(00\)00014-2](https://doi.org/10.1016/S0037-0738(00)00014-2)
- HILTON, R.G., GAILLARDET, J., CALMELS, D., BIRCK, J. (2014) Geological respiration of a mountain belt revealed by the trace element rhenium. *Earth and Planetary Science Letters* 403, 27–36. <https://doi.org/10.1016/j.epsl.2014.06.021>
- HILTON, R.G., WEST, A.J. (2020) Mountains, erosion and the carbon cycle. *Nature Reviews Earth and Environment* 1, 284–299. <https://doi.org/10.1038/s43017-020-0058-6>
- HOLLINGSWORTH, E.H., ELLING, F.J., BADGER, M.P.S., PANCOST, R.D., DICKSON, A.J., REES-OWEN, R.L., PAPADOMANOLAKI, N.M., PEARSON, A., SLUIJS, A., FREEMAN, K.H., BACZYNSKI, A.A., FOSTER, G.L., WHITESIDE, J.H., INGLIS, G.N. (2024) Spatial and Temporal Patterns in Petrogenic Organic Carbon Mobilization During the Paleocene-Eocene Thermal Maximum. *Paleoceanography and Paleoclimatology* 39. <https://doi.org/10.1029/2023PA004773>
- JIN, S., KEMP, D.B., SHEN, J., YIN, R., JOLLEY, D.W., VIEIRA, M., HUANG, C. (2024) Spatiotemporal distribution of global mercury enrichments through the Paleocene-Eocene Thermal Maximum and links to volcanism. *Earth-Science Reviews* 248, 104647. <https://doi.org/10.1016/j.earscrev.2023.104647>
- JOHN, C.M., BOHATY, S.M., ZACHOS, J.C., SLUIJS, A., GIBBS, S., BRINKHUIS, H., BRALOWER, T.J. (2008) North American continental margin records of the Paleocene-Eocene thermal maximum: Implications for global carbon and hydrological cycling. *Paleoceanography* 23, 1–20. <https://doi.org/10.1029/2007PA001465>
- KIRTLAND TURNER, S. (2018) Constraints on the onset duration of the Paleocene-Eocene Thermal Maximum. *Philosophical Transactions of the Royal Society A* 376, 1–16. <https://doi.org/10.1098/rsta.2017.0082>
- KOPP, R.E., SCHUMANN, D., RAUB, T.D., POWARS, D.S., GODFREY, L.V., SWANSON-HYSELL, N.L., MALOOF, A.C., VALL, H. (2009) An Appalachian Amazon? Magnetofossil evidence for the development of a tropical river-like system in the mid-Atlantic United States during the Paleocene-Eocene thermal maximum. *Paleoceanography* 24, 1–17. <https://doi.org/10.1029/2009PA001783>
- LYONS, S.L., BACZYNSKI, A.A., BABILA, T.L., BRALOWER, T.J., HAJEK, E.A., KUMP, L.R., POLITES, E.G., SELF-TRAIL, J.M., TRAMPUSH, S.M., VORNLOCHER, J.R., ZACHOS, J.C., FREEMAN, K.H. (2019) Palaeocene–Eocene Thermal Maximum prolonged by fossil carbon oxidation. *Nature Geoscience* 12, 54–60. <https://doi.org/10.1038/s41561-018-0277-3>
- SCHINGROSS, J.S., REPASCH, M.N., HOVIUS, N., SACHSE, D., LUPKER, M., FUCHS, M., HALEVY, I., GRÖCKE, D.R., GOLOMBEK, N.Y., HAGHFOUR, N., EGLINTON, T.I., ORFEO, O., SCHLEICHER, A.M. (2021) The fate of fluvially-deposited organic carbon during transient floodplain storage. *Earth and Planetary Science Letters* 561, 116822. <https://doi.org/10.1016/j.epsl.2021.116822>
- SELF-TRAIL, J.M., ROBINSON, M.M., BRALOWER, T.J., SESSA, J.A., HAJEK, E.A., KUMP, L.R., TRAMPUSH, S.M., WILLARD, D.A., EDWARDS, L.E., POWARS, D.S., WANDLESS, G.A. (2017) Shallow marine response to global climate change during the Paleocene-Eocene Thermal Maximum, Salisbury Embayment, USA. *Paleoceanography* 32, 710–728. <https://doi.org/10.1002/2017PA003096>
- SLUIJS, A., SCHOUTEN, S., PAGANI, M., WOLTERING, M., BRINKHUIS, H., DICKENS, G.R., HUBER, M., REICHAERT, G., STEIN, R., MATTHIESSEN, J., LOURENS, L.J., PEDENTCHOUK, N., BACKMAN, J., MORAN, K. (2006) Subtropical Arctic Ocean temperatures during the Palaeocene/Eocene thermal maximum. *Nature* 441, 610–613. <https://doi.org/10.1038/nature04668>
- SLUIJS, A., RÖHL, U., SCHOUTEN, S., BRUMSACK, H.-I., SANGIORGI, F., SINNINGHE DAMSTÉ, J.S., BRINKHUIS, H. (2008) Arctic late Paleocene–early Eocene paleoenvironments with special emphasis on the Paleocene-Eocene thermal maximum (Lomonosov Ridge, Integrated Ocean Drilling Program Expedition 302). *Paleoceanography* 23, 1–17. <https://doi.org/10.1029/2007PA001495>
- SOULET, G., HILTON, R.G., GARNETT, M.H., ROYLANDS, T., KLOTZ, S., CROISSANT, T., DELLINGER, M., LE BOUTELLIER, C. (2021) Temperature control on CO₂ emissions from the weathering of sedimentary rocks. *Nature Geoscience* 14, 665–671. <https://doi.org/10.1038/s41561-021-00805-1>
- SPARKES, R.B., HOVIUS, N., GALY, A., KUMAR, R.V., LIU, J.T. (2013) Automated analysis of carbon in powdered geological and environmental samples by Raman spectroscopy. *Applied Spectroscopy* 67, 779–788. <https://doi.org/10.1366/12-06826>
- SPARKES, R.B., MAHER, M., BLEWETT, J., DOČRUĽ SELVER, A., GUSTAFSSON, Ö., SEMILETOV, I.P., VAN DONGEN, B.E. (2018) Carbonaceous material export from Siberian permafrost tracked across the Arctic Shelf using Raman spectroscopy. *Cryosphere* 12, 3293–3309. <https://doi.org/10.5194/tc-12-3293-2018>
- SPARKES, R.B., HOVIUS, N., GALY, A., KUMAR, R. V., LIU, J.T. (2020) Survival of graphitized petrogenic organic carbon through multiple erosional cycles. *Earth and Planetary Science Letters* 531, 115992. <https://doi.org/10.1016/j.epsl.2019.115992>
- TIERNEY, J.E., ZHU, J., LI, M., RIDGWELL, A., HAKIM, G.J., POULSEN, C.J., WHITEFORD, R.D.M., RAE, J.W.B., KUMP, L.R. (2022) Spatial patterns of climate change across the Paleocene–Eocene Thermal Maximum. *Proceedings of the National Academy of Sciences of the United States of America* 119, e2205326119. <https://doi.org/10.1073/pnas.2205326119>
- ZEEBE, R.E. (2013) What caused the long duration of the Paleocene-Eocene Thermal Maximum? *Paleoceanography* 28, 440–452. <https://doi.org/10.1002/palo.20039>
- ZEEBE, R.E., LOURENS, L.J. (2019) Solar System chaos and the Paleocene–Eocene boundary age constrained by geology and astronomy. *Science* 365, 926–929. <https://doi.org/10.1126/science.aax0612>

Enhanced petrogenic organic carbon oxidation during the Paleocene-Eocene thermal maximum

E.H. Hollingsworth, R.B. Sparkes, J.M. Self-Trail, G.L. Foster, G.N. Inglis

Supplementary Information

The Supplementary Information includes:

- Table S-1 and S-2
- Figure S-1 and S-2
- Supplementary Information References

Table S-1 Number of disordered carbon vs. graphitised carbon spectra from SDB, with duplicate results in parenthesis. The disordered and graphitised carbon were separated based on peak burial temperatures, which were calibrated using the R2 and RA2 peak area ratio (see Sparkes *et al.*, 2013). The time intervals are as follows: Pre-PETM, PETM (onset/body), Recovery, and Post-PETM, based on Hollingsworth *et al.* (2024) and references therein. The pre-onset Excursion (POE) in the Pre-PETM interval is isolated using the definition from Babila *et al.* (2022).

| Time interval | Approx. sample depth (m) | Disordered carbon | Graphitised carbon |
|---------------|--------------------------|-------------------|--------------------|
| Post-PETM | 186.6 | 5 | 5 |
| Post-PETM | 188 | 7 | 3 |
| Recovery | 190.99 | 6 | 3 |
| Recovery | 192.57 | 5 | 5 |
| Recovery | 193.3 | 5 | 5 |
| Recovery | 193.88 | 2 | 7 |
| Recovery | 195.07 | 5 | 5 |
| Recovery | 196.41 | 3 | 7 |
| PETM | 196.93 | 3 | 7 |
| PETM | 197.21 | 2 (4) | 8 (6) |
| PETM | 199.52 | 3 | 7 |
| PETM | 199.83 | 4 | 6 |
| PETM | 200.28 | 2 | 8 |
| PETM | 200.83 | 2 | 7 |
| PETM | 201.47 | 3 | 6 |
| PETM | 202.08 | 3 | 7 |
| PETM | 202.37 | 4 (9) | 6 (1) |
| PETM | 202.68 | 7 | 3 |
| PETM | 202.98 | 5 | 4 |
| PETM | 203.06 | 7 (7) | 3 (2) |
| PETM | 203.3 | 6 | 3 |
| PETM | 203.88 | 9 | 1 |
| Pre-PETM | 204.26 | 9 | 1 |
| Pre-PETM | 204.49 | 8 | 2 |
| Pre-PETM | 204.84 | 8 | 2 |
| Pre-PETM | 205.12 | 9 (9) | 1 (1) |
| Pre-PETM | 205.4 | 8 | 2 |
| Pre-PETM | 205.44 | 8 | 2 |
| Pre-PETM | 205.74 | 7 | 3 |
| POE | 206.04 | 8 | 2 |
| POE | 206.35 | 9 | 1 |
| POE | 206.41 | 5 | 4 |
| POE | 206.68 | 9 | 1 |
| POE | 207.04 | 5 | 5 |
| POE | 207.08 | 7 | 3 |
| Pre-PETM | 208.83 | 7 | 3 |

Table S-2 Number of disordered carbon vs. graphitised carbon spectra from ACEX. The disordered and graphitised carbon were separated based on peak burial temperatures, which were calibrated using the R2 and RA2 peak area ratio (see Sparkes *et al.*, 2013). The time intervals are as follows: Pre-PETM, PETM (onset/body), Recovery, and Post-PETM, based on Hollingsworth *et al.* (2024) and references therein.

| Time interval | Depth (mcd) | Freeze-dried | Oven-dried | Disordered carbon | Graphitised carbon |
|---------------|-------------|--------------|------------|-------------------|--------------------|
| Post-PETM | 378.14 | Yes | | 9 | 1 |
| Recovery | 378.69 | | Yes | 10 | 0 |
| Recovery | 380.73 | Yes | | 10 | 0 |
| Recovery | 381.56 | Yes | | 9 | 1 |
| PETM | 382.15 | | Yes | 9 | 1 |
| PETM | 382.94 | | Yes | 8 | 1 |
| PETM | 383.87 | | Yes | 10 | 0 |
| PETM | 385.11 | | Yes | 10 | 0 |
| Pre-PETM | 388.03 | | Yes | 10 | 0 |
| Pre-PETM | 388.87 | Yes | | 10 | 0 |
| Pre-PETM | 389.75 | | Yes | 10 | 0 |
| Pre-PETM | 390.78 | Yes | | 10 | 0 |

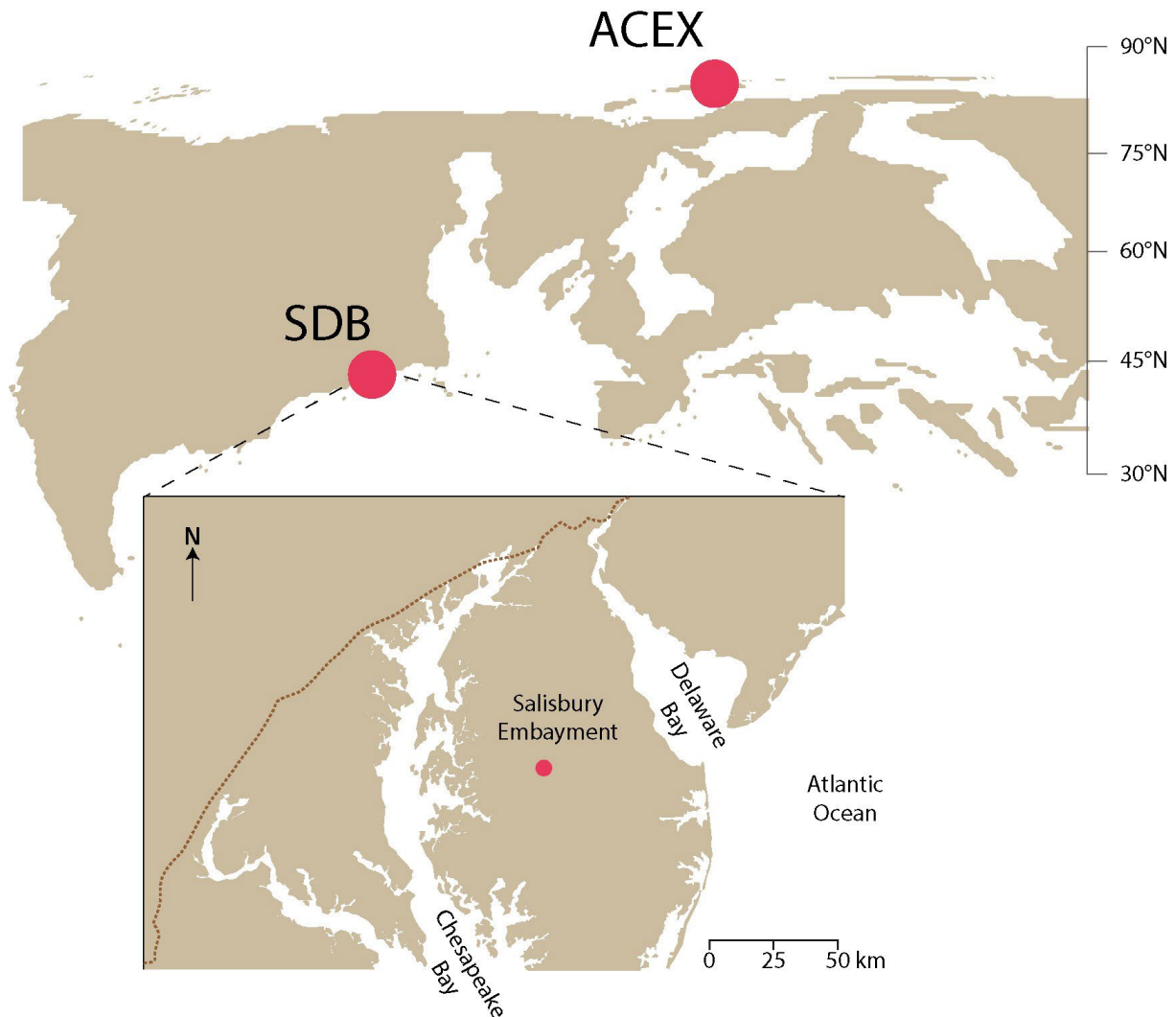


Figure S-1 Location of the Arctic Coring Expedition (ACEX; 82.81°N, 66.91°E) and South Dover Bridge (SDB; 41.39°N, 59.48°W) during the PETM (palaeo-latitudes based on mantle reference frame; Hollis *et al.*, 2019). Top panel: representation of the palaeogeography of the Northern Hemisphere 56 Ma, adapted from Carmichael *et al.* (2017). Bottom panel: the mid-Atlantic Coastal Plain with the modern coastline and Fall Line (brown dashed line).

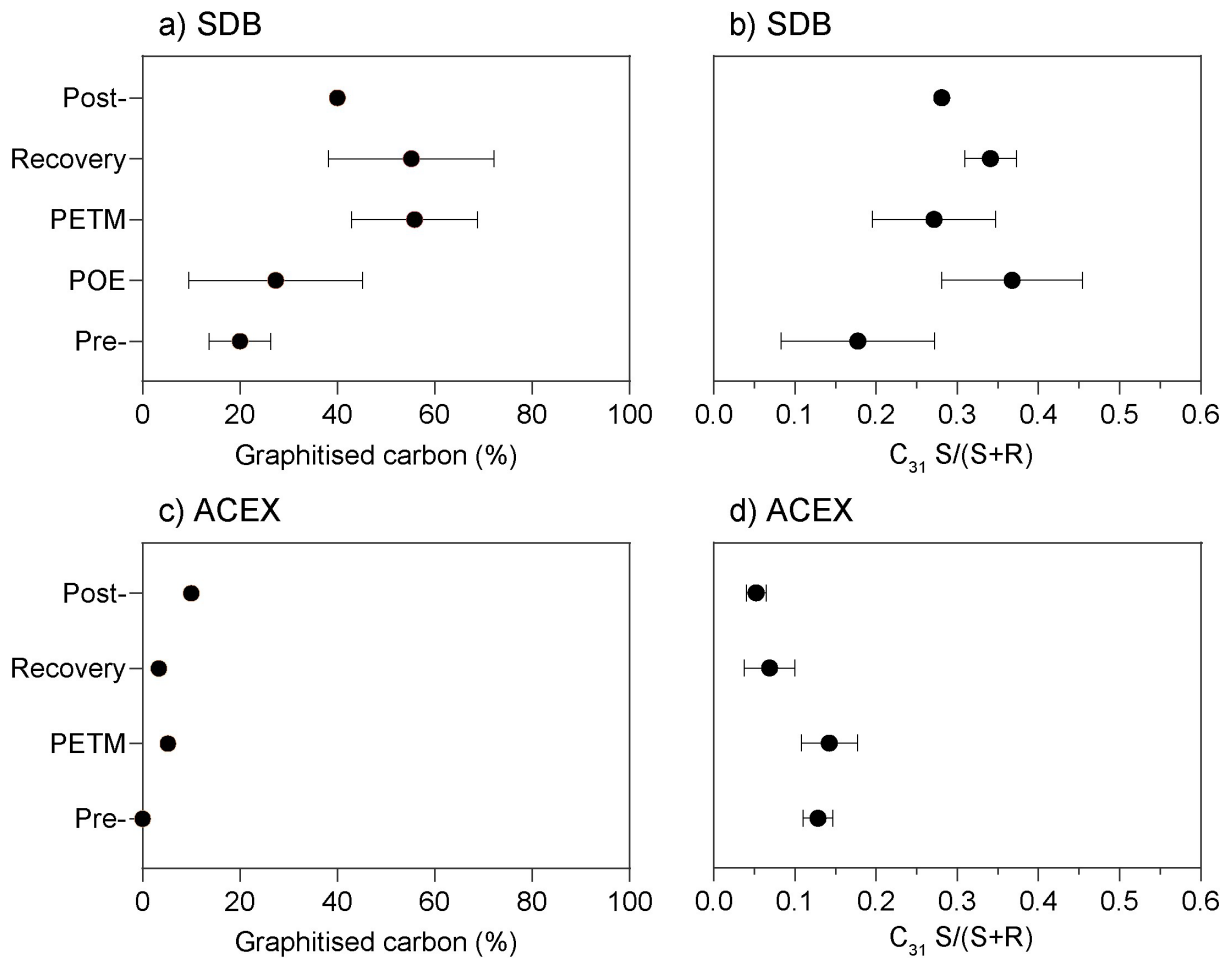


Figure S-2 Mean percentages of graphitised carbon (this study) and mean values of the C_{31} homohopane $22S/(22S+22R)$ ratio (Lyons *et al.*, 2019; Hollingsworth *et al.*, 2024), from (a-b) SDB and (c-d) ACEX. The time intervals are as follows: Pre-PETM, PETM (onset and body), Recovery, and Post-PETM (see Hollingsworth *et al.*, 2024 and references therein). At SDB, the POE in the Pre-PETM interval is isolated using the definition from Babila *et al.* (2022). The uncertainty is displayed as the 95 % confidence interval of the mean, with error bars not included when sample size is <4.

Supplementary Information References

- Babila, T.L., Penman, D.E., Standish, C.D., Doubrava, M., Bralower, T.J., *et al.* (2022) Surface ocean warming and acidification driven by rapid carbon release precedes Paleocene-Eocene Thermal Maximum. *Science Advances* 8. <https://doi.org/10.1126/sciadv.abg1025>
- Carmichael, M.J., Inglis, G.N., Badger, M.P.S., Naafs, B.D.A., Behrooz, L., Rimmelzwaal, S., Monteiro, F.M., Rohrsen, M., Farnsworth, A., Buss, H.L., Dickson, A.J., Valdes, P.J., Lunt, D.J., Pancost, R.D. (2017) Hydrological and associated biogeochemical consequences of rapid global warming during the Paleocene-Eocene Thermal Maximum. *Global and Planetary Change* 157, 114–138. <https://doi.org/10.1016/j.gloplacha.2017.07.014>
- Hollingsworth, E.H., Elling, F.J., Badger, M.P.S., Pancost, R.D., Dickson, A.J., *et al.* (2024) Spatial and Temporal Patterns in Petrogenic Organic Carbon Mobilization During the Paleocene-Eocene Thermal Maximum. *Paleoceanography and Paleoclimatology* 39. <https://doi.org/10.1029/2023PA004773>
- Hollis, C.J., Dunkley Jones, T., Anagnostou, E., Bijl, P.K., Cramwinckel, M.J., *et al.* (2019) The DeepMIP contribution to PMIP4: Methodologies for selection, compilation and analysis of latest Paleocene and early Eocene climate proxy data, incorporating version 0.1 of the DeepMIP database. *Geoscientific Model Development* 12, 3149–3206. <https://doi.org/10.5194/gmd-12-3149-2019>
- Lyons, S.L., Baczynski, A.A., Babila, T.L., Bralower, T.J., Hajek, E.A., *et al.* (2019) Palaeocene–Eocene Thermal Maximum prolonged by fossil carbon oxidation. *Nature Geoscience* 12, 54–60. <https://doi.org/10.1038/s41561-018-0277-3>
- Sparkes, R.B., Hovius, N., Galy, A., Kumar, R.V., Liud, J.T. (2013) Automated analysis of carbon in powdered geological and environmental samples by Raman spectroscopy. *Applied Spectroscopy* 67, 779–788. <https://doi.org/10.1366/12-06826>